Reconstruction of 3D precipitation measurements from FY-3G MWRI-RM imaging and sounding channels

Yunfan Yang[1,2], Wei Han[3,4], Haofei Sun[1,2], Jun Li[5], Jiapeng Yan[4], and Zhiqiu Gao[1,2]

[1]State Key Laboratory of Atmospheric Boundary Layer Physics and Atmospheric Chemistry (LAPC), Institute of Atmospheric Physics, Chinese Academy of Sciences, Beijing, China
[2]University of Chinese Academy of Sciences, Beijing, China
[3]CMA Earth System Modeling and Prediction Centre (CEMC), China Meteorological Administration, Beijing, China
[4]State Key Laboratory of Severe Weather (LaSW), Chinese Academy of Meteorological Sciences, China Meteorological Administration, Beijing, China
[5]National Satellite Meteorological Center, China Meteorological Administration, Beijing, 100081, China

Correspondence: Wei Han (hanwei@cma.gov.cn)

Abstract. FengYun 3G satellite (FY-3G), China's first precipitation measurement satellite, was launched on April 17, 2023. FY-3G carries an advanced multi-channel microwave radiance imager-rainfall measurement (MWRI-RM) system, which, compared to the previous GPM/GMI, includes more sounding channels. Additionally, a Ka/Ku-band dual-frequency precipitation measurement radar (PMR) onboard FY-3G provides 3D observations of severe precipitation systems. Due to the high cost
5 and hardware limitations of precipitation radars, most precipitation-affected satellite observations rely on passive data. Deep learning methods have become effective tools to bridge these two types of observations. In this study, we proposed a deep convolutional neural network (CNN) to reconstruct PMR-Ku reflectivity profiles (VPR) based on MWRI-RM multi-channel radiances across different precipitation scenarios and analyzed the effects of dual oxygen absorption sounding channels and polarization differences (PD) on reconstruction outcomes. Experiments showed that dual oxygen absorption sounding channels
10 improved VPR accuracy, especially over land, reducing RMSE by 17.42%. Including PD further enhanced accuracy, reducing RMSE by 23.54%, while also demonstrating excellent capability in precipitation identification, achieving an F1 score of 0.904. Applying the models to Typhoon Khanun and the extreme precipitation event in Beijing further demonstrated the benefits of dual oxygen sounding channels and PD, even for reflectivity contaminated by ground clutter.

1 Introduction

15 precipitation plays a critical role in the Earth's climate system and water cycle, influencing everything from global climate patterns to agricultural productivity and water resources (Huang et al., 2023). Understanding the instantaneous structure and global distribution of precipitation is essential for comprehending changes in the global climate. Satellite observations, combining passive (PMW) and active microwave sensors (AMW), have become vital tools in enhancing our understanding of these processes (Dubovik et al., 2021). They provide comprehensive coverage over diverse terrains, including oceans, deserts, and
20 high plateaus, thus deepening our knowledge of atmospheric dynamics on a global scale (Hou et al., 2014).
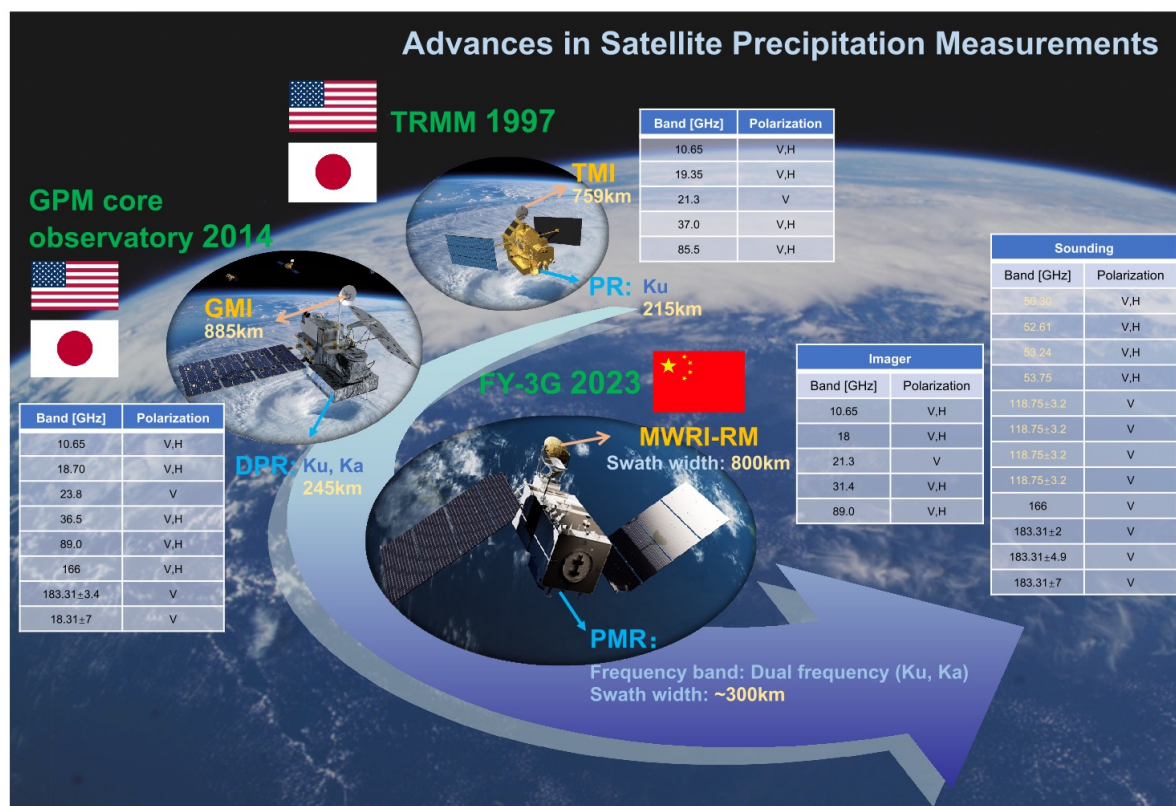
Figure 1. Comparison of channel configurations and swath widths of microwave imagers, as well as frequency configurations and swath widths of precipitation radars, on three typical precipitation measurement satellites.

Fig. 1 illustrates the progression of space-based precipitation measurements, which began with the launch of the Tropical Rainfall Measuring Mission (TRMM) in 1997, a joint initiative between Japan and the United States (Simpson et al., 1996). TRMM was equipped with a suite of sensors, including the Precipitation Radar (PR) and the TRMM Microwave Imager (TMI), enabling combined passive-active microwave observations and allowing for detailed analyses of the macro- and microphysical structures of precipitating clouds (Kummerow et al., 1998). Building on TRMM's legacy, the United States initiated the Global Precipitation Measurement (GPM) mission, launching the GPM Core satellite (GPMCO) in 2014 (Draper et al., 2015). Orbiting at an altitude of 407 km with a 65° inclination, GPMCO carrying a Ka/Ku-band dual-frequency precipitation radar (DPR) and a wideband (10–183 GHz) multifrequency microwave imager (GMI). The GMI and DPR also serve as a transfer standard for calibrating precipitation retrieval algorithms by establishing a reference for other satellites in the GPM constellation. The mission's expanded capabilities facilitated a deeper understanding of the three-dimensional structures and global distribution of precipitation (Draper and Newell, 2018).

In response to these developments and the significance of hazardous weather events like typhoons, heavy rains, and severe convective storms in China, the China Meteorological Administration, in collaboration with the China Aerospace Science

and Technology Corporation, initiated the development of the Fengyun-3 (FY-3) series of precipitation satellites. On April 16,
35 2023, at 09:36 Beijing time, China's first dedicated precipitation measurement satellite, FY-3G, was successfully launched. FY-3G is equipped with the passive Microwave Radiance Imager-Rainfall Measurement (MWRI-RM) and the active Precipitation Measurement Radar (PMR), enhancing the detection of atmospheric, cloud, and precipitation structures and advancing the scientific understanding of precipitation and cloud microphysics (Zhang et al., 2023a). Building on the microwave imager (MWRI) technology of the FY-3 satellite series, MWRI-RM integrates microwave sounding and imaging capabilities with 26
40 channels ranging from 10 to 183 GHz (He et al., 2024). As shown in Fig. 1, in addition to carrying channels similar to those on previous microwave imagers like TMI and GMI, MWRI-RM includes additional sounding channels around the 50 GHz and 118GHz oxygen absorption bands. The dual oxygen absorption sounding channels offer several unique advantages. Firstly, due to their distinct absorption and scattering characteristics (Bauer and Mugnai, 2003; Bauer et al., 2005), the combination of 50 GHz and 118 GHz channels can effectively identify clouds and precipitation (Hu and Weng, 2022). Furthermore, cloud
45 structures can be retrieved at various height levels, enabling three-dimensional observations (Han et al., 2015). Secondly, compared to traditional window channels, the dual oxygen absorption sounding channels are less sensitive to land surface emissivity, making them more suitable for all-surface observing and monitoring of the atmosphere (Prigent et al., 2005). Finally, these channels can also provide rich and valuable information about the atmospheric thermal structure (Carminati et al., 2021). The inclusion of auxiliary sounding channels near the 183 GHz water vapor strong lines further enhances MWRI-
50 RM's capability on profiling the atmospheric humidity and precipitation (Laviola and Levizzani, 2011; Laviola et al., 2013). A preliminary assessment of MWRI-RM/FY-3G brightness temperatures (BT) using double difference (DD) analysis, based on simultaneous measurements from GMI, suggests that MWRI-RM has the performance comparable to GMI for most channels, particularly the channels at 166 GHz and 183 GHz (He et al., 2024).

Previous studies have shown that there is a strong correlation between active and passive microwave observations. For in-
55 stance, active observations have been used to validate precipitation profiles retrieved from passive radiance data (Bauer and Mugnai, 2003; Kummerow et al.), and combined active-passive microwave observations have been instrumental in retrieving comprehensive precipitation products and classifying precipitation types (Grecu et al., 2004, 2016; Das et al., 2022). The complementary data from both methods provide valuable insights into precipitation characteristics. Despite the ability of radar to provide detailed three-dimensional (3D) observations, the high cost of deploying scanning radars on satellites and their
60 limited swath width means that most satellite-based precipitation observations still rely heavily on PMW data (Bauer et al., 2005; Guilloteau et al., 2018). PMW, though less precise than AMW by only gathering two-dimensional (2D) radiance, provides a cost-effective and practical alternative. They offer extensive global coverage with wider swaths, making them essential for continuous monitoring of precipitation. Moreover, their multi-channel capabilities allow for an indirect inference of vertical precipitation profiles, thereby partially compensating for their inherent limitations (Guilloteau and Foufoula-Georgiou,
65 2020). Therefore, identifying the direct relationship between PMW and AMW observations is crucial and valuable. However, accurately correlating the 2D passive data with 3D radar measurements involves complex nonlinear relationships that are challenging to decipher using traditional methods. The emergence of deep learning has introduced new possibilities for addressing these challenges (Zhu et al., 2017; Yuan et al., 2020; Zhou et al., 2023). By leveraging extensive observational datasets, deep

learning models can learn to map the complex relationships between passive microwave measurements and active radar data, enabling the reconstruction of detailed three-dimensional precipitation structures. This approach has been evidenced by recent research in reconstructing cloud structures observed by cloud radar using satellite imagery data (Haynes et al., 2022; Wang et al., 2023a, b). For instance, Brüning et al. (2024) combined high-resolution satellite imagery with radar data by developing a Res-UNet model to generate 3D cloud structures. However, reconstruction work involving precipitation measurement radar observations remains scarce. Previous efforts have explored the potential of deep neural networks to map the relationships between the GPM Microwave Imager (GMI) and the Dual-frequency Precipitation Radar (DPR) (Yang et al., 2024), but these have been initially limited to specific precipitation scenarios due to limited spectral channels of GMI (Turk et al., 2018), for example, lack of sounding channels.

Building on this foundation, our study employs observations from MWRI-RM and PMR on the newly launched FY-3G satellite. By introducing dual oxygen sounding channels at 50 GHz and 118 GHz, the MWRI-RM facilitates the reconstruction of land precipitation and improves the accuracy of measurements related to the position and thickness of melting layers. Furthermore, the inclusion of auxiliary channels near the 183 GHz water vapor line may enhance the reconstruction of reflectivity for ice-phase particles. This breadth of channels offers a unique opportunity to extract a more comprehensive array of precipitation observations from PMR (Guilloteau and Foufoula-Georgiou, 2020), enabling more detailed reconstructions of precipitation systems than possible.

This study leverages deep learning techniques to reconstruct 3D precipitation structures across different scenarios—over oceans, land, and in non-precipitating conditions by utilizing the full capability of FY-3G/ MWRI-RM, with focus on assessing how the new sounding channels influence the performance of reconstruction. We aim to enhance the accuracy and reliability of precipitation measurements through combined PMW and AMW observations, ensuring that the information provided by the MWRI-RM's comprehensive channel suite translates into a significant improvement in the reconstruction of radar reflectivity profiles for improving high impact weather (HIW) monitoring and prediction.

2 Data and Methodology

2.1 Data Source and Characteristics

The primary data utilized in this study was acquired from the FY-3G precipitation satellite launched by China in 2023. Operating in a unique low-inclination, non-sun-synchronous, inclined orbit at a nominal altitude of 407 kilometers and an inclination of $50°\pm1°$, the satellite covers the global mid-to-low latitude regions (Fig. 2a). It is equipped with two important precipitation observation payloads which are the Ka/Ku Dual-frequency Precipitation Radar (PMR) and the Microwave Radiance Imager-Rainfall Measurement (MWRI-RM). These instruments are crucial for monitoring catastrophic weather systems like typhoons and heavy rainfall.

PMR: Serving the core payload of FY-3G, which provides 3D structural data on precipitation systems, the PMR is a single-polarization one-dimensional (1D) phased-array radar with a cross-track scanning mechanism (Gu et al., 2022). It covers a ground swath width of 303 kilometers and offers a horizontal resolution of 5 kilometers at the nadir and a vertical resolution of

250 meters, as depicted in Fig. 2b and Fig. 3. Additionally, it is capable of detecting precipitation with a minimum reflectivity of 12 dBZ.

MWRI-RM: A significant payload of the FY-3G satellite, the MWRI-RM has 17 frequency points ranging from 10.65

105 GHz to 183 GHz, which includes dual-polarized channels in the 10-89 GHz spectrum, totalling 26 channels with spatial resolutions ranging from 5 to 25 kilometers. Detailed channel information for the MWRI RM can be found in Table 4 in Zhang et al. (2023a). Employing a conical scanning regime with imaging channels and sounding channels having incidence angles of 53°±1° and 50°±1° respectively, MWRI-RM has an effective observation swath of 800 kilometers, as illustrated in Fig. 2b and Fig. 3. This instrument captures passive microwave radiation from the Earth's surface, yielding information on precipitation,

110 atmospheric water vapor, cloud liquid content, path-integrated liquid water thickness, melting layer height and thickness, sea surface wind speed, and more (Zhang et al., 2023a).

The Level 1 products of PMR and MWRI-RM can be downloaded from the FENGYUN Satellite Data Center website (https://satellite.nsmc.org.cn).

(a)   (b)
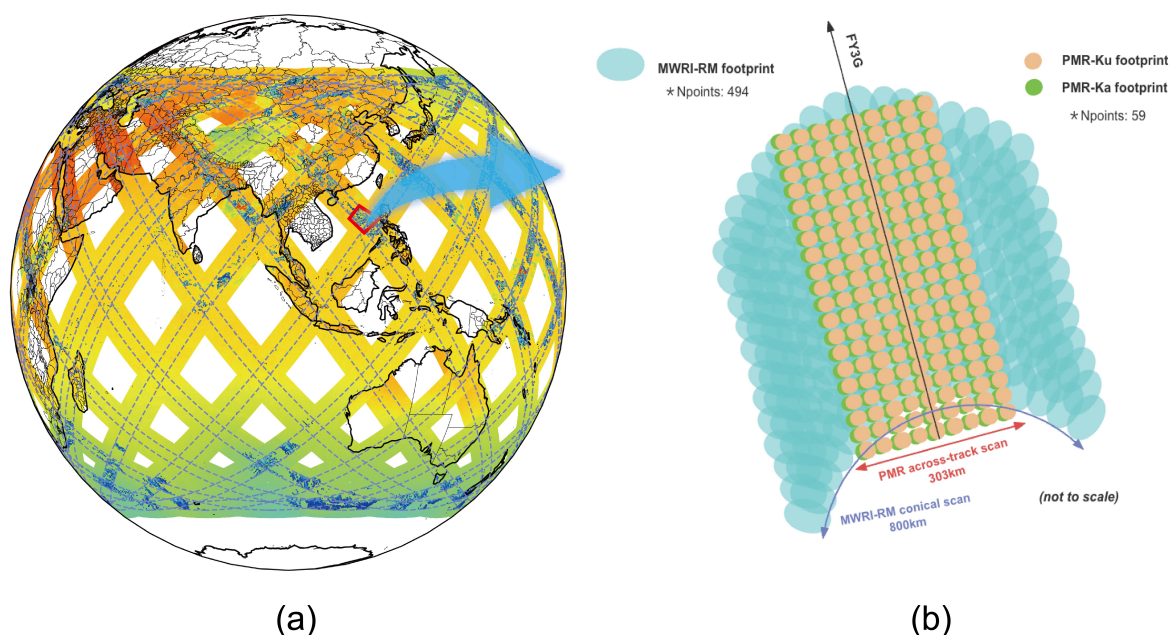
Figure 2. (a) The brightness temperatures from the MWRI-RM's 52.61 GHz vertical polarization channel and PMR's reflectivity at approximately 4 km above ground, recorded on July 31, 2023. The blue dashed line indicates the PMR scanning swath. (b) The viewing geometry of the MWRI-RM and PMR, with footprint sizes and numbers that do not correspond to actual observations but represent a conceptual example. Adapted from Fig 1 in Turk et al. (2021).

2.2 Data Preprocessing

115 The operationally calibrated MWRI-RM Level 1 data and PMR Level 1 data have been released since 23 October 2023. The first release of data spanning from 23 October to 31 November 2023 is used here for the preliminary research. During the data preprocessing phase, the spatial positions of MWRI-RM data were first unified. Due to the angular discrepancy in the observational geometry of the MWRI-RM's two arrays of feedhorns (S1 and S2), we applied the nearest neighbor method to adjust the spatial positioning of these two sets of data for consistency. Polarization Difference (PD) is introduced as a key

120 analytical variable, calculated from the difference between the brightness temperatures (Tbs) of vertically and horizontally polarized channels (PD = Tb_V - Tb_H). This parameter aids in revealing the shape and size distribution of hydrometeors, providing unique perspectives on precipitation processes (Geer et al., 2021). For the MWRI-RM, polarization differences were derived from nine channel pairs across frequencies: 10.65, 18.7, 23.8, 36.5, 50.30, 52.61, 53.24, 53.75, and 89 GHz. Each frequency channel offers distinctive insights into atmospheric conditions and hydrometeor characteristics.

125 In processing the PMR radar reflectivity profiles, special attention was given to mitigating the influence of ground clutter, which escalates with incidence angle. Reflectivity profiles with local zenith angles less than 2° were selectively analyzed to minimize the interference from ground clutter, which affects altitudes up to approximately 1.1 km. This approach is based on the observation that ground clutter's detrimental effects on radar measurements intensify with greater zenith angles, thus necessitating an angular threshold to uphold data quality (Kubota et al., 2016; Shimizu et al., 2023). To balance the number of

130 clear-sky and cloudy pixels, we only selected radar bins below 8 km, considering the cloud tops of most precipitation clouds are below this altitude (Yang et al., 2024). This helps model capture the essential data while minimizing noise from higher altitudes that might not be as relevant for precipitation analysis. The final VPR dimension encompasses 136 bins ranging from 1.1 to 8 km. Radar reflectivity values were also adjusted to account for the presence of noise (absence of precipitation signals), sidelobe clutter, and ground clutter. Radar bins affected by noise were assigned a baseline value of 10 dBZ, supported by

135 statistical evidence indicating that precipitation echoes typically exceed 12 dBZ. This selected baseline value helps distinguish between non-precipitating and precipitating conditions without significantly altering the overall distribution of reflectivity values, thereby maintaining the integrity of the reconstruction process. Bins impacted by sidelobe and ground clutter were marked as invalid (NaN) to prevent their potential negative influence on the reconstruction outcome.

The subsequent step in data preprocessing involved aligning the MWRI-RM data with PMR observations. This alignment

140 was based on matching MWRI-RM and PMR footprints closest in space and within a scan time difference of less than 80 seconds (Yang et al., 2024). Considering the different scanning modes of the PMR (cross-track scanning) and MWRI-RM (conical scanning), there are inherent differences in the spatial coverage of their observations (Fig. 2b). Although we performed nearest-neighbor matching for the ground footprints, the actual atmospheric volumes observed by each instrument are not identical. To best match the atmospheric conditions observed by both instruments, a patch extraction technique was

145 employed, centered on the matched MWRI-RM footprint (Fig. 3). This ensures that the atmospheric column observed by the PMR is always intersected by multiple MWRI-RM scanning beams. Consequently, the MWRI-RM Tb patch encompasses the atmospheric state information of the column observed by the PMR. This approach aligns the data from the two sensors more

effectively, enhancing the model's ability to accurately interpret and utilize these observations. Our preliminary studies have indicated that a patch size of 15×15 offers the most optimal reconstruction performance (Yang et al., 2024). This choice allows

150   for the inclusion of sufficient relevant atmospheric information and ensures effective observation matching. Consequently, this study utilizes exclusively patches of this specified size for analysis.
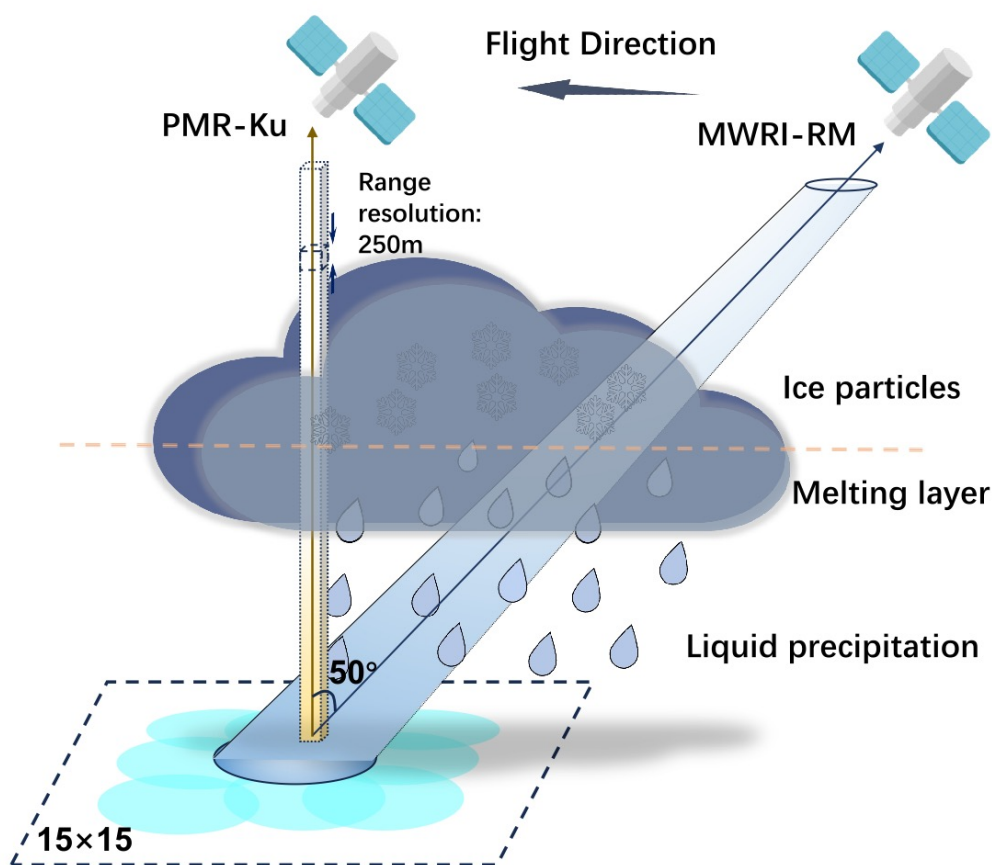
Figure 3. Schematic representation of viewing volumes of MWRI-RM and PMR in the atmosphere, illustrating the patch extraction technique employed to the matched footprint of MWRI-RM.

Given the natural scarcity of precipitation events compared to non-precipitation conditions, an oversampling of non-precipitation samples was performed. This procedure aimed to balance the quantity of precipitation and non-precipitation samples, providing a more equitable dataset for model training and evaluation. Following the above preprocessing, a total of 838,591 sample

155   pairs were generated. To facilitate model training and validation, these sample pairs were divided into training and testing subsets, with 80% of the samples allocated for training purposes and the remaining 20% designated for testing. Prior to training,

all inputs were standardized. Additionally, since the label VPR exhibited a skewed distribution, a logarithmic transformation was applied. This preprocessing step is essential for reducing the impact of outliers and ensuring that the model learns from a more uniform dataset, thereby enhancing the reliability and accuracy of the predictions. The overall preprocessing flow is summarized in Fig. 4.

2.3 Deep Learning Model Architecture

In our investigation, we adopt a deep learning architecture that diverges from the mixed model approach reported by Yang et al. (2024). Unlike their study, which explored the benefits of a combined CNN-MLP approach for integrating Tb patches from multiple channels and ancillary temperature profile data, our model emphasizes the potency of CNNs in discerning the vertical structure of atmospheric temperature directly from the advanced sounding channels, particularly those near the oxygen absorption bands. These sounding channels are sensitive to the temperature profile, thus potentially reducing the necessity for separate profile information processing.

Table 1. Architectural Details of CNN Models.

Type	Parameters	Output
Input	-	$C \times 15 \times 15$
Conv	$C \times 32 \times 3 \times 3$	$32 \times 15 \times 15$
B.R.D	2×32	$32 \times 15 \times 15$
Conv	$32 \times 64 \times 3 \times 3$	$64 \times 15 \times 15$
B.R.D	2×64	$64 \times 15 \times 15$
Conv	$64 \times 128 \times 3 \times 3$	$128 \times 15 \times 15$
B.R.D	2×128	$128 \times 15 \times 15$
FC	$200 \times 128 \times 15 \times 15$	200
FC	138×200	138

To validate our CNN-based model's effectiveness, we focus on its application using MWRI-RM's enriched dataset. Detailed specifications of the CNN model configuration are delineated in Table 1. In Table 1, C denotes the number of input channels For experiments Exp_Baseline_14, Exp_FullChannel_26, and Exp_PolarDiffEnhanced_35, C is 14, 26, and 35, respectively. The term B.R.D represents a sequence of three layers: Batch Normalization, Rectified Linear Unit (ReLU) activation layer, and Dropout. For all cases, dropout is applied with a probability of p = 0.2. Model optimization follows a rigorous training protocol utilizing the Adam optimizer with Mean Squared Error (MSE) as the loss function(Kingma and Ba, 2017). To critically evaluate

the influence of various channel configurations and feature inputs on the model's ability to reconstruct radar reflectivity, we
orchestrated a series of controlled experiments as shown in Fig. 4, each designed to illuminate different facets of model
performance:

1. Baseline Experiment (Exp_Baseline_14): The baseline experiment eschews the oxygen absorption sounding channels,
relying on 14 input channels to ascertain the model's foundational ability to reconstruct radar reflectivity without the nuanced
atmospheric temperature information that the omitted channels might offer. The implications of this configuration are particu-
larly pertinent for the delineation of temperature profiles and the identification of atmospheric layers such as the melting layer,
which are integral to the precise reconstruction of radar reflectivity.

2. Full Channel Experiment (Exp_FullChannel_26): By employing all 26 input channels inclusive of the oxygen absorption
bands, this experiment seeks to harness the comprehensive channel information available. It aims to utilize the atmospheric
temperature profiles that the oxygen absorption channels provide, which is pivotal for a refined identification of precipitation
events and could significantly enhance the detection capabilities for weak precipitation and the delineation of melting layers.

3. Polarization Difference Enhanced Experiment (Exp_PolarDiffEnhanced_35): Building upon the full channel input, this
experiment incorporates additional Tb polarization difference data, bringing the total to 35 input channels. This inclusion is
intended to fortify the model's acuity in recognizing diverse precipitation characteristics, especially in differentiating between
precipitation types and capturing precipitation structure with heightened detail.

By setting these experiments against the backdrop of a consistent architectural framework, our study provides a rigorous
evaluation and better understanding of the data-driven enhancements offered by the MWRI-RM's extended channel set. This
methodical exploration is crucial for unraveling the full potential of deep learning in advancing meteorological observation and
forecasting techniques.

2.4 Evaluation metrics

To quantify the reconstruction accuracy of the model, we employed three statistical indices: Mean Bias Error (MBE), Standard
Deviation (STD) of the predictive error, and Root Mean Square Error (RMSE). Each metric offers a distinct dimension of the
model's performance.

The MBE is indicative of the average bias in the model's predictions, where a value of zero represents a perfect bias-free
model. It is computed as follows:

$$\text{MBE} = \frac{1}{n} \sum_{i=1}^{n} (R_i - O_i) \tag{1}$$

Where R_i is the reconstructed value, O_i is the observed value, and n is the number of data points. This metric reveals
whether the model tends to overpredict or underpredict the observed values, providing insight into systematic deviations.

The STD of the predictive error measures the spread of these errors around the mean error, indicating the variability within
the dataset:

$$\text{STD} = \sqrt{\frac{1}{n-1}\sum_{i=1}^{n}(R_i - O_i - \text{MBE})^2} \tag{2}$$

Here, the term $R_i - O_i - \text{MBE}$ represents the deviation of each individual reconstruction error from the MBE. The STD elucidates the volatility in reconstruction performance and identifies the degree to which individual reconstructions deviate from the average bias.

Finally, the RMSE assesses the magnitude of the error, penalizing larger discrepancies more severely, thus highlighting the model's precision:

$$\text{RMSE} = \sqrt{\frac{1}{n}\sum_{i=1}^{n}(R_i - O_i)^2} \tag{3}$$

The RMSE is especially useful as it relates directly to the data's scale, offering an unambiguous interpretation of the model's predictive capability.

F1 Score evaluates the model's precision and recall, crucial for applications where distinguishing between event types (precipitating vs. non-precipitating) carries significant operational consequences (Vakili et al., 2020). The F1 Score is particularly useful in situations where the classes are imbalanced, such as in meteorological predictions where non-precipitation events are more frequent. It balances the model's precision and recall, providing a single measure of accuracy in identifying precipitation events.

$$F1 = 2 \times \left(\frac{\text{Precision} \times \text{Recall}}{\text{Precision} + \text{Recall}}\right) \tag{4}$$

$$\text{Precision} = \frac{\text{TP}}{\text{TP} + \text{FP}} \tag{5}$$

$$\text{Recall} = \frac{\text{TP}}{\text{TP} + \text{FN}} \tag{6}$$

where TP, FP, and FN represent the numbers of true positives, false positives, and false negatives, respectively.

By utilizing these indices, we can deliver a rigorous and comprehensive evaluation of our model's predictive accuracy, providing a balanced overview of both central tendency and variability in the model's performance. This multifaceted approach ensures a robust assessment, crucial for validating the model's applicability to operational forecasting scenarios.
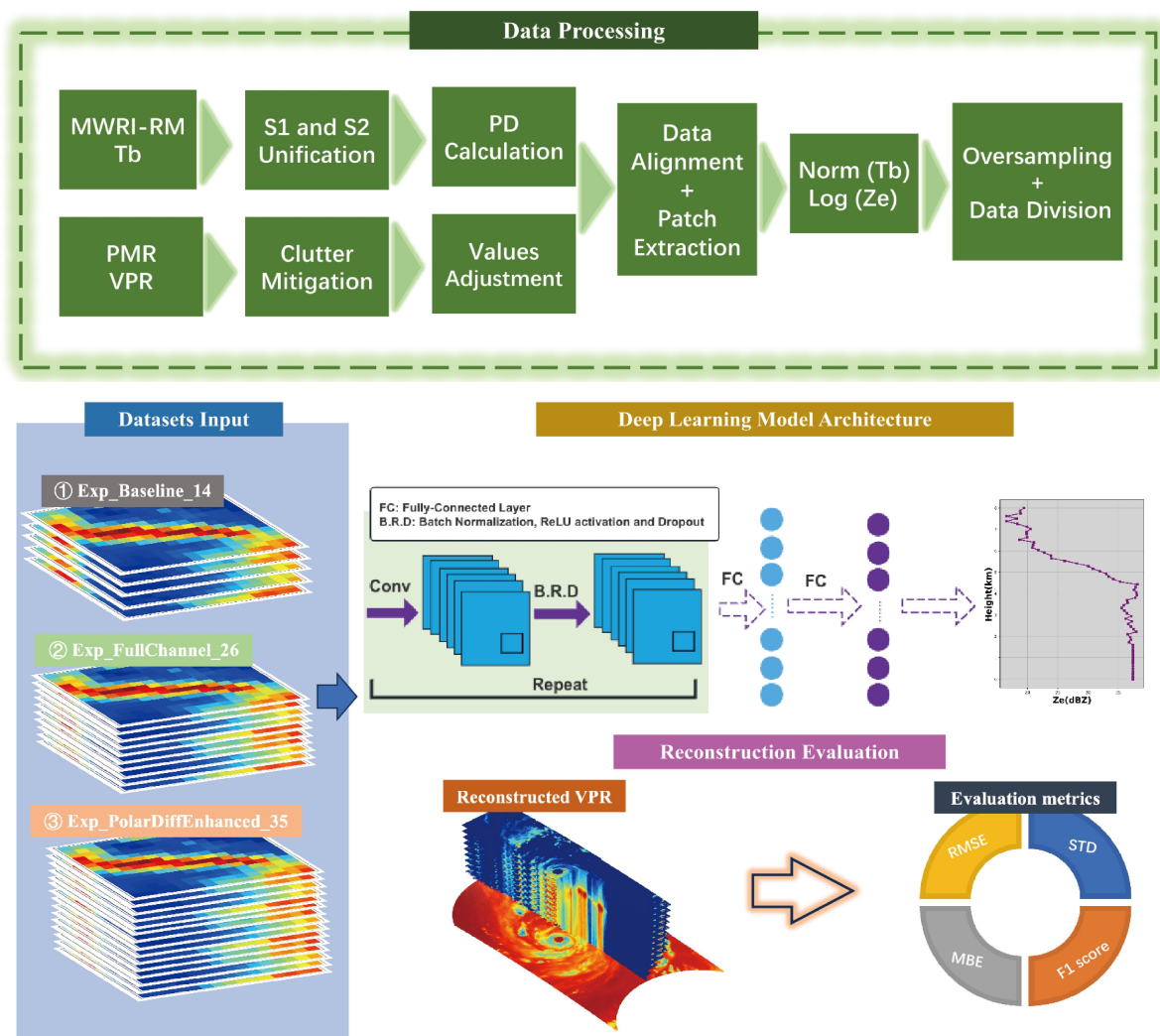
Figure 4. Diagram of Data Processing Workflow, Model Architecture, and Evaluation Metrics.

3 Results

3.1 Reconstruction Performance and Evaluation

In this section, we conduct a comprehensive evaluation of the performance of three experiments—Exp_Baseline_14, Exp_FullChannel_26, and Exp_PolarDiffEnhanced_35—to elucidate the effects of dual oxygen absorption channels and polarization differences on reconstruction outcomes. Fig. 5 illustrates the variations in MBE, RMSE, and STD across different height levels for three scenarios: oceanic precipitation, land precipitation, and non-precipitation under the conditions of the three experiments. Ad-

ditionally, Table. 2 provides detailed numerical values for evaluation metrics under different scenarios for each of the three experiments, offering a thorough quantitative analysis of model performance.

Table 2.

Evaluation Metrics for Three Experiments Across Different Precipitation Scenarios. The table provides detailed numerical values for oceanic precipitation, land precipitation, and non-precipitation conditions for each experiment.

Experiments	Scenarios	Evaluation Metrics			
		RMSE	MBE	STD	F1 Score
Exp_Baseline_14	Oceanic Precipitation	3.498	0.429	3.471	0.889
	Land Precipitation	5.305	1.769	5.002	0.889
	Non-Precipitation	0.433	-0.094	0.422	/
Exp_Baseline_26	Oceanic Precipitation	3.298	0.499	3.261	0.898
	Land Precipitation	4.381	0.855	4.297	0.898
	Non-Precipitation	0.370	-0.054	0.366	/
Exp_Baseline_35	Oceanic Precipitation	3.046	0.353	3.025	0.904
	Land Precipitation	4.056	0.641	4.005	0.904
	Non-Precipitation	0.371	-0.068	0.364	/

A general trend observed is the reduction of errors with increasing altitude. However, the errors at the melting layer are also

235 significant, highlighting a crucial area for model refinement, particularly in adjusting to phase changes in precipitation. The comparison between oceanic and land precipitation scenarios reveals greater reconstruction errors over land. This discrepancy is largely attributed to the interference of land surface emissivity at low-frequency channel bands, which compromises the channels' ability to convey accurate precipitation information (Munchak and Skofronick-Jackson, 2013). Such limitations underscore the challenges faced by the model in land precipitation scenarios due to the reduced effectiveness of low-frequency

240 channel observations in these environments. With the integration of dual oxygen absorption sounding channels, there is a notable improvement in the accuracy of precipitation reflectivity reconstruction, especially over land, with RMSE reduced by 17.4%. This enhancement is also evident near the melting layer in all scenarios, underscoring the sounding channels' sensitivity to atmospheric temperature structures. This feature is instrumental in refining the model's ability to accurately map precipitation structures by leveraging the scattering signal of precipitation and the temperature profiles provided by the oxygen

245 absorption sounding channels. The incorporation of Tb polarization difference further enhances the model's performance. This aligns with previous studies that highlighted the critical role of polarization difference in refining precipitation reflectivity reconstructions, as polarization differences between channels are indicative of the phase and type of precipitation, enhancing the model's ability to accurately delineate between different hydrometeorological conditions (Yang et al., 2024). Despite these

improvements, the model tends to underestimate precipitation reflectivity across scenarios, as indicated by a generally positive
250 MBE, suggesting a systematic low bias in precipitation estimation.

In non-precipitation conditions, the model shows minimal error, with RMSE values less than 1 dBZ. The slight difference between the background value and the minimal precipitation threshold (2 dBZ) reinforces the model's capability to accurately detect the absence of precipitation. Moreover, the F1 Scores for the three experiments—Exp_Baseline_14, Exp_FullChannel_26, and Exp_PolarDiffEnhanced_35, are 0.889, 0.898, and 0.904, respectively. These scores confirm the model's efficacy in dis-
255 tinguishing between precipitating and non-precipitating conditions, illustrating its robustness and potential applicability in operational use.

3.2 Model Performance Evaluation During Extreme Precipitation Events

In this part of the paper, we focus on evaluating the model's reconstruction capabilities during two extreme precipitation events: Typhoon Khanun in 2023 and the extreme precipitation in Beijing and its surrounding areas from July 29 to July 31,
260 2023 (Fowler et al., 2024). These events caused significant impacts on human life and activities, providing challenging yet informative scenarios for testing the model's precision and robustness. Fig. 6 and 7 provide a comparative analysis of the three-dimensional reflectivity structures of Typhoon Khanun as observed at 05:30 UTC on July 31, 2023 and extreme precipitation around the southern part of Beijing and its surrounding areas as observed at 23:18 UTC July 30, 2023, across three different experimental models. The figure contrasts the observed reflectivity values (panels a-c) with the reconstructed data obtained
265 from three experiments: Exp_Baseline_14 (e-f), Exp_FullChannel_26 (g-i), and Exp_PolarDiffEnhanced_35 (j-l). Each set of panels is organized to include three key perspectives: the 3D reflectivity structure (left column), the horizontal distribution at 4 km altitude (middle column), and the vertical cross-section along points A and B (right column). As shown in Fig. 6, the 3D reflectivity profile from PMR data revealed decreasing reflectivity values with altitude, typical of frozen precipitation forms such as snow, graupel, and frozen drops commonly found in the cores of active thunderstorms. Ground clutter limited
270 the observation range at the lowest altitudes, but the model, trained on reflectivity profiles with incidence angles less than 2°, reconstructed a more complete reflectivity profile, minimizing ground clutter effects. This demonstrates the model's capability to reconstruct reflectivity impacted by clutter, an essential feature for accurate storm characterization.

For a detailed horizontal analysis of the precipitation system, we chose a reflectivity cross-section at 4 km above ground, where the influence of ground clutter was minimal, revealing a more comprehensive view of the precipitation system. PMR
275 data showed the highest reflectivity values located mainly to the south and east of Khanun's center, with moderate to heavy rainfall surrounding the eye and a prominent rainband to the northwest. Additionally, a vertical cross-section along a line from point A to point B (both directly beneath the satellite track) was analyzed to assess the vertical structure of the precipitation system. This cross-section clearly displayed a prominent bright band (BB) in this melting layer, characterized by a peak in reflectivity, a common feature where falling snow begins to melt into rain, enhancing the radar signal (Xie et al., 2024).
280 Analysis of the reconstruction results from different experiments showed that while all models accurately reconstructed the overall structure of the precipitation system, there were noticeable differences in detail. The Exp_Baseline_14 generally underestimated reflectivity values in the northwestern rainbands while overestimating those east of Khanun's center (Fig. 6d,
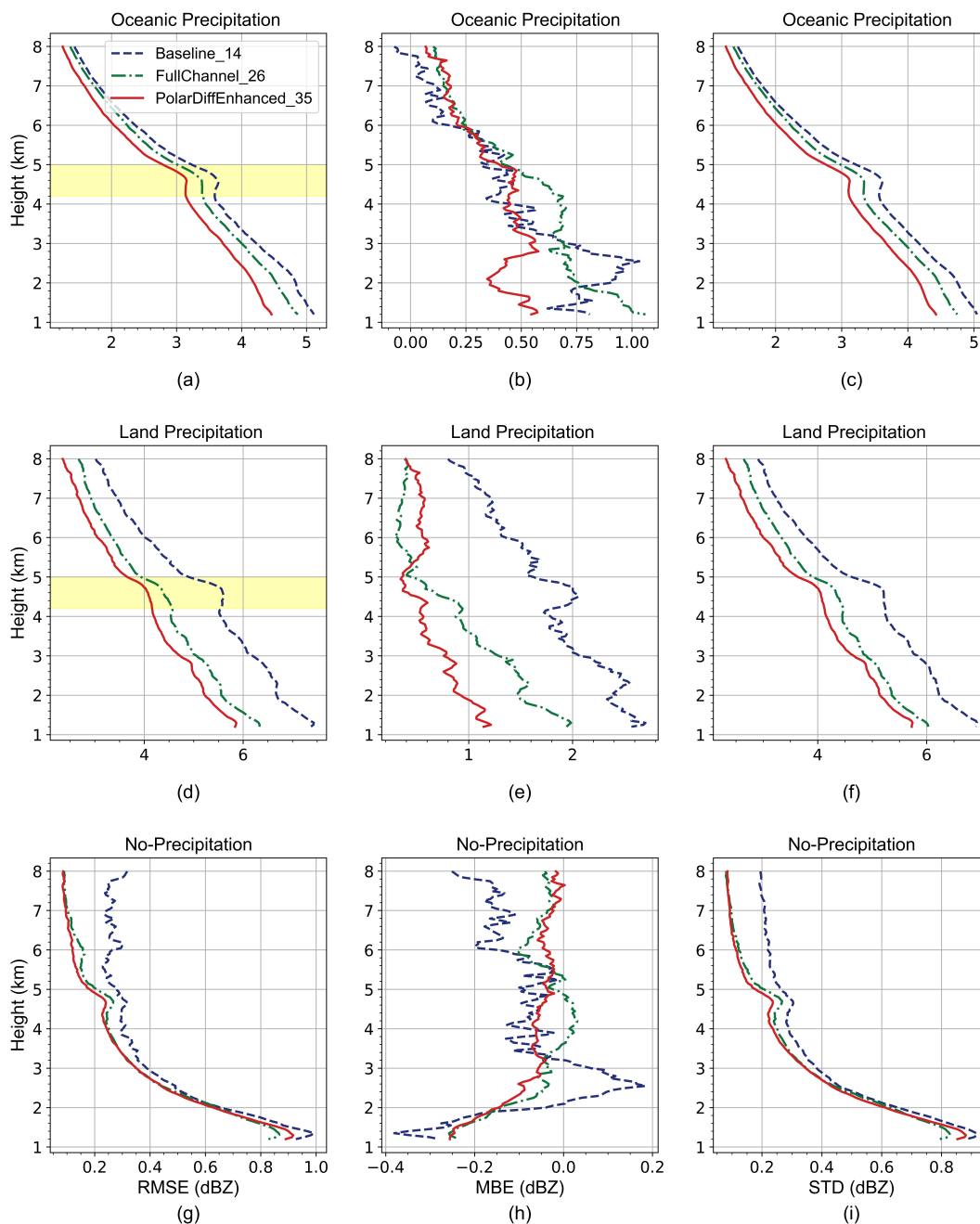
Figure 5. Comparison of RMSE (left), MBE (middle), and STD (right) Error Profiles for Reflectivity Reconstruction Across Different Precipitation Scenarios Using Three Experiments: Exp_Baseline_14 (purple line), Exp_FullChannel_26 (green line), and Exp_PolarDiffEnhanced_35 (red line). Highlighted shading indicates the position of the melting layer in each scenario.

e). The reconstructed melting layer structure was overly smooth, indicating a lack of detailed temperature information, which is crucial for accurately capturing this feature. The Exp_FullChannel_26 provided a clearer understanding of the melting

285 layer structure as depicted in Fig. 6i. However, it exhibited an overall weaker reflectivity reconstruction. This attenuation in performance is likely due to the influence of atmospheric absorption at the oxygen absorption bands. As the frequency approaches these strong oxygen absorption bands, the background microwave Tbs intensify, obscuring the contributions from raindrops (Bauer and Mugnai, 2003; Qin et al., 2020). This stronger background radiation makes the precipitation signals less distinct, particularly in regions of light rain, thereby complicating the task of effectively reconstructing the reflectivity profiles

290 from passive microwave data. In contrast, the Exp_PolarDiffEnhanced_35 results were closer to observations in detail, yet still slightly overestimated reflectivity values east of Khanun's center (Fig. 6j, k). Its representation of the melting layer was more accurate, closely matching actual observations (Fig. 6l). However, as with the Typhoon Khanun event, all experiments showed some discrepancies in the position of the melting layer, typically positioned lower than observed, likely affected by the inherent fuzziness of the radiative signals impacting the vertical resolution and detail in the reconstructions.

295 The satellite's flight over Beijing occurred during extreme precipitation, with local precipitation reaching up to 482 mm in areas such as Mentougou and Fangshan in Beijing, and Baoding and Shijiazhuang in Hebei, as illustrated in Fig. 7. Despite severe ground clutter and complex terrain effects causing significant observation gaps below 2 km, high reflectivity values consistent with ground station reports were still observable in Beijing's central and southern regions. At 4 km, PMR observations showed high reflectivity predominantly in the central and southern parts of Beijing, northeastern Hebei, and northeastern

300 Shanxi, although the edge of the satellite track was affected by terrain, leading to missing reflectivity data in these mountainous regions. In the vertical structure analysis along a cross-section from point A to point B in southern Beijing, the bright band (BB) in this melting layer occurred around 5 km. Similar to the findings from the Khanun typhoon, all experiments reconstructed the overall precipitation system structure accurately but differed in detail. The Exp_Baseline_14 accurately captured high reflectivity in southern Beijing but underestimated it in central and northeastern Hebei. It failed to reconstruct the melting

305 layer, indicating that temperature information from oxygen absorption channels is crucial for accurately depicting vertical precipitation structures over land, consistent with earlier model evaluations. The Exp_FullChannel_26, although capturing major high reflectivity areas, generally reconstructed weaker reflectivity values and underestimated the reflectivity within the melting layer. The Exp_PolarDiffEnhanced_35 provided the most accurate detail, closely reconstructing each high reflectivity area and more accurately depicting the vertical melting layer features.

310 Based on the above evaluation, the Exp_PolarDiffEnhanced_35 model demonstrates superior performance in reconstructing the horizontal distribution, vertical structure, and intensity of reflectivity for both oceanic and terrestrial precipitation. In this section, we utilize the Exp_PolarDiffEnhanced_35 model to reconstruct the reflectivity across the entire MWRI-RM swath to gain a more comprehensive view of precipitation systems. Fig. 8a and c show the reconstructed reflectivity of Typhoon Khanun across the entire MWRI-RM swath. Compared to the actual observations from PMR-Ku, we can observe a very complete three-

315 dimensional structure of the typhoon. For instance, the well-formed spiral rainbands accompanied by intense reflectivity in the southwest of Typhoon Khanun's eyewall have been well reconstructed, a feature not evident in the PMR-Ku observations. Similarly, Fig. 8b and d present a more complete reflectivity distribution of a terrestrial precipitation system. In addition to
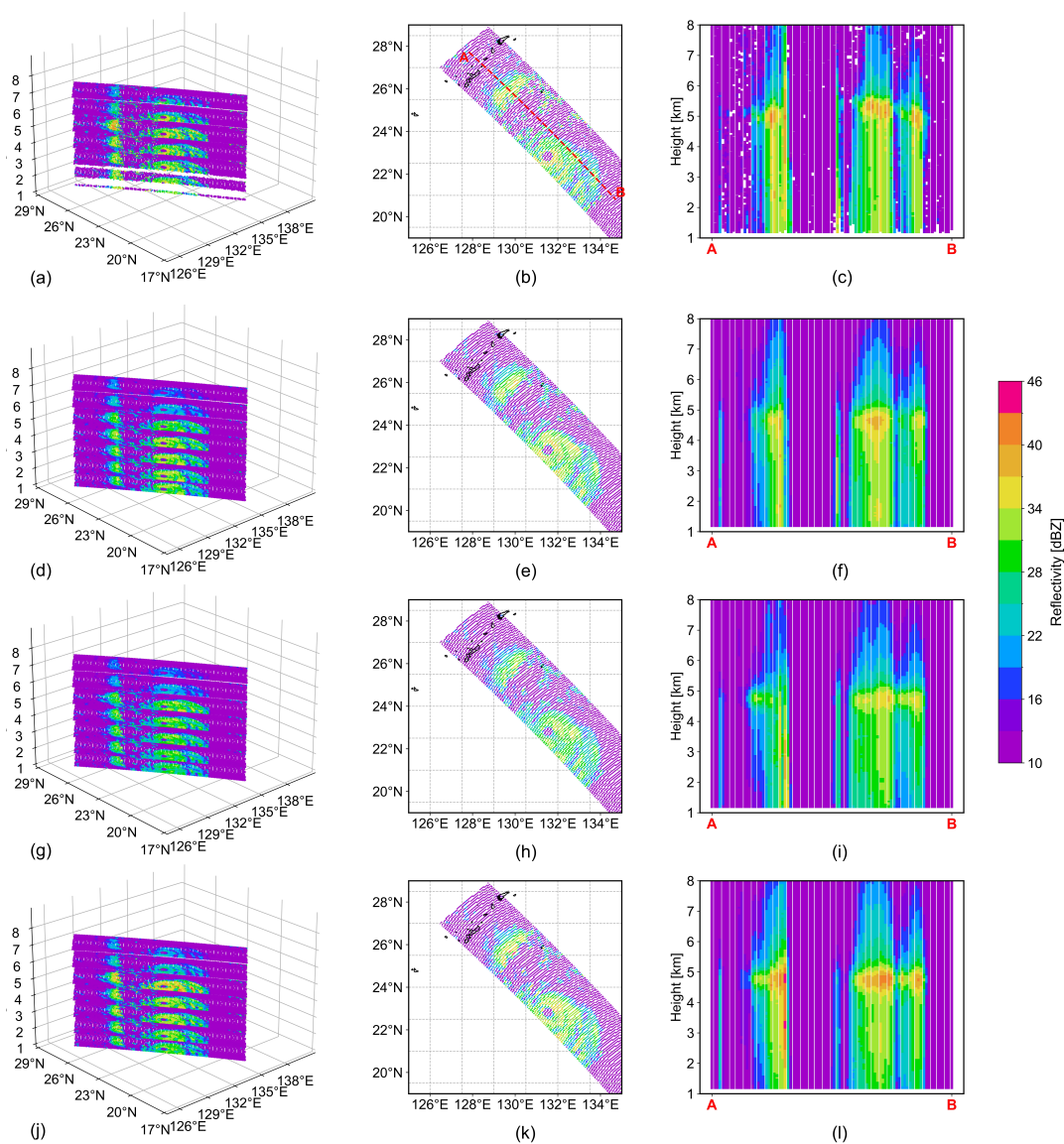
Figure 6. Comparative Analysis of Three-Dimensional Reflectivity Structures of Typhoon Khanun (05:30 UTC July 31, 2023) Across Three Experiments. The panels compare observed values (a-c) with reconstructed data from Exp_Baseline_14 (e-f), Exp_FullChannel_26 (g-i), and Exp_PolarDiffEnhanced_35 (j-l) models. Each set includes 3D reflectivity structure (left), horizontal distribution at 4km (middle), and vertical cross-section along points A and B (right).
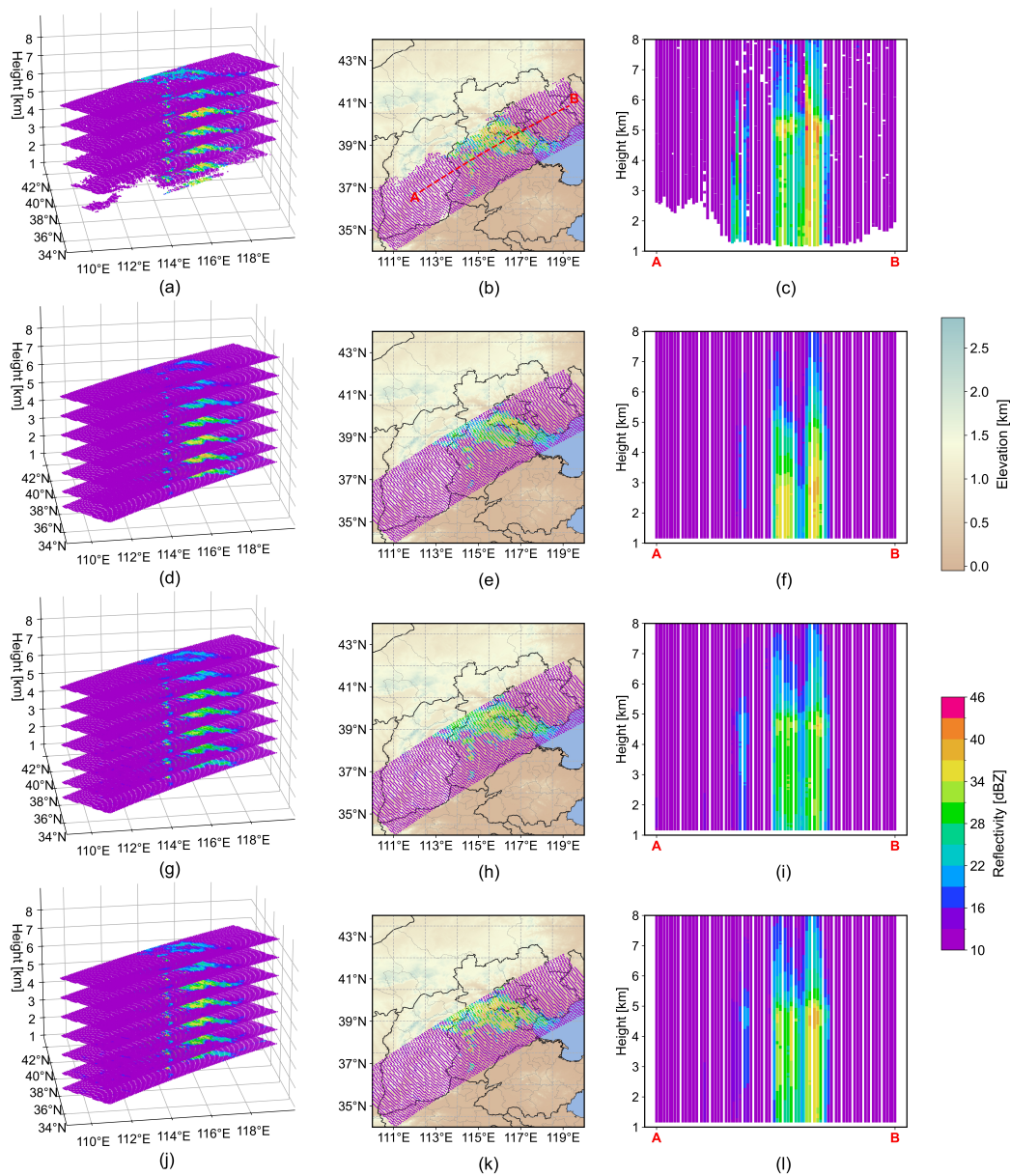
Figure 7. Same as Fig. 6, but for extreme precipitation around the southern part of Beijing and its surrounding areas (23:18 UTC July 30, 2023).

the precipitation echoes observed by PMR-Ku over southern Beijing, central Hebei, and Tianjin, the MWRI-RM swath reveals precipitation echoes over northern Hebei, northern Shanxi, and parts of Inner Mongolia adjacent to Shanxi.
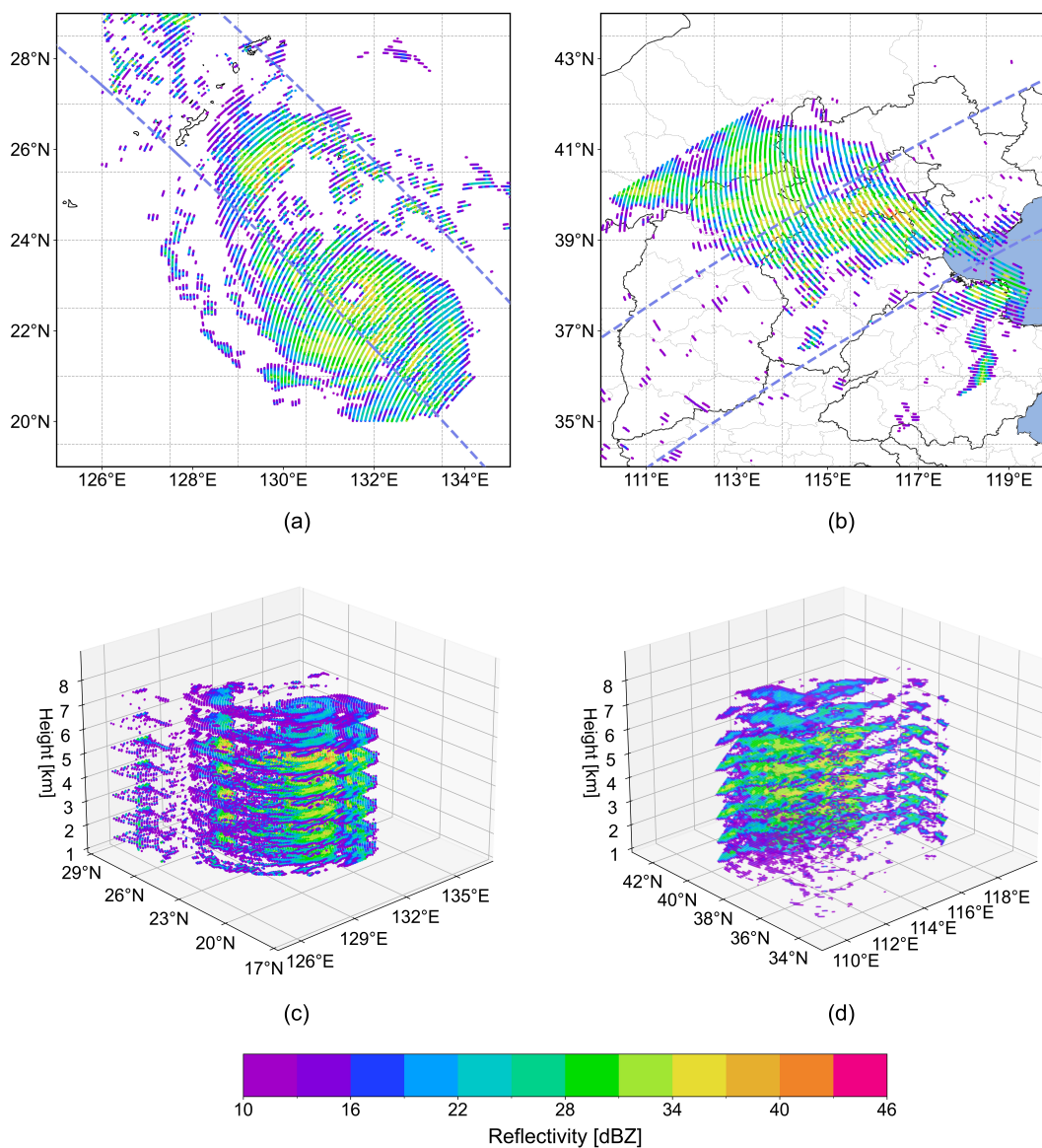
Figure 8. Exp_PolarDiffEnhanced_35 model reconstructions of reflectivity from Typhoon Khanun (05:30 UTC July 31, 2023; left colunm) and extreme precipitation around the southern part of Beijing and its surrounding areas (23:18 UTC July 30, 2023; right colunm) within the MWRI-RM swath.

320   To further evaluate the accuracy of the model's reconstructed reflectivity, we compared the reconstructed Ku-band reflectivity distribution of the land precipitation with the ground-based radar reflectivity distribution at the same altitude. Fig. 9

represents the radar constant altitude plan position indicator (CAPPI) products derived from 99 dual-polarization S-band operational weather radars within and surrounding the study area. However, ground-based radars do not cover remote areas such as northern Shanxi and parts of Inner Mongolia adjacent to Shanxi. The reconstructed precipitation reflectivity distributions

325   based on MWRI-RM observations are consistent with actual ground-based radar observations. This consistency demonstrates the model's ability to leverage MWRI-RM data to depict detailed and complete precipitation structures.
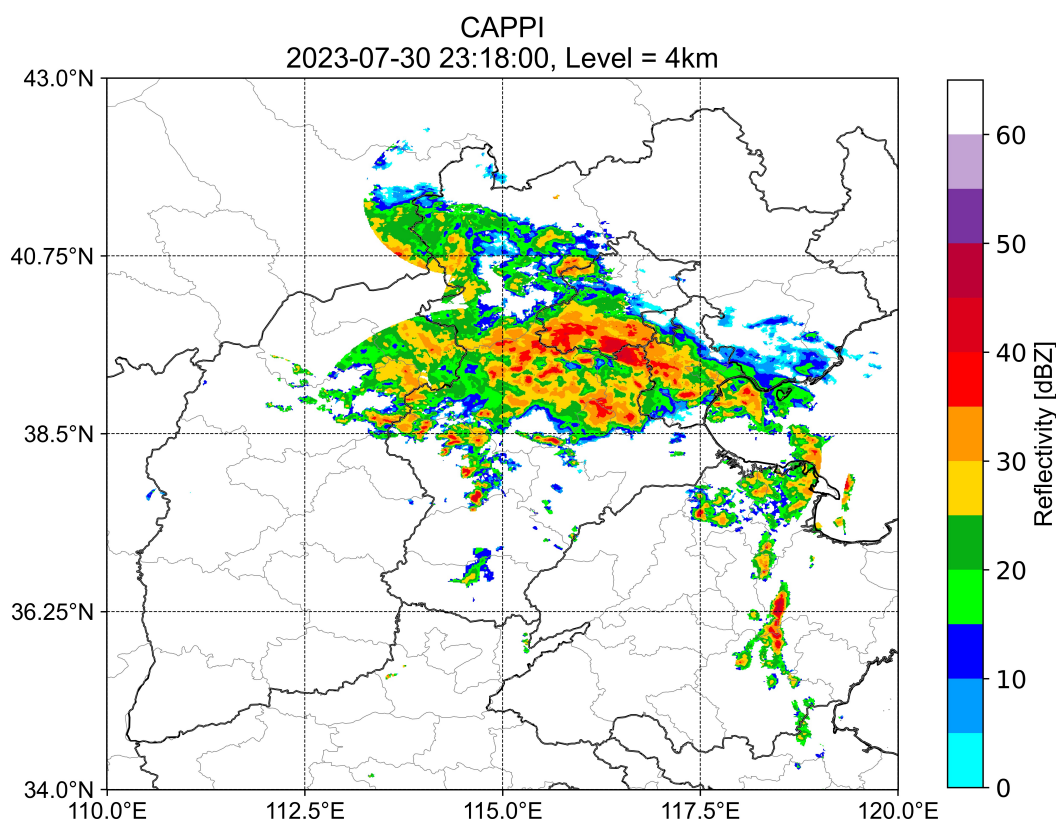
Figure 9. Reflectivity of precipitation from southern Beijing and its surroundings observed by ground-based S-band radar.

4   Conclusions and discussions

The study demonstrates the significant impact of incorporating additional sounding channels and polarization differences in enhancing precipitation reconstruction models. It also introduces an innovative use of analytical methods for evaluation, which

330   is critical in assessing the efficacy of new channels dedicated to precipitation detection and contributes to the ongoing advancement of remote sensing technology.

     Three experiments: Exp_Baseline_14, Exp_FullChannel_26, and Exp_PolarDiffEnhanced_35, were evaluated, revealing the effects of dual oxygen absorption sounding channels and polarization differences on reconstruction outcomes. The find-

ings indicate a general trend of error reduction with increasing altitude, though significant errors persist at the melting layer,
335   highlighting a need for model refinement in adjusting to phase changes in precipitation. Reconstruction errors are greater over
land compared to oceanic scenarios due to land surface emissivity interference with low-frequency channels, emphasizing the
challenges in land precipitation scenarios.

The integration of dual oxygen absorption sounding channels significantly improved the accuracy of precipitation reflectivity
reconstruction, particularly over land, with RMSE reduced by 17.42%. This improvement underscores the channels' sensitivity
340   to atmospheric temperature structures, enhancing the model's ability to map precipitation structures accurately. Additionally,
the incorporation of brightness temperature polarization differences further improved the model's performance, aligning with
previous studies on the role of polarization in refining precipitation reflectivity reconstructions. Despite these enhancements,
the model exhibited a systematic low bias in reflectivity estimation, as indicated by a generally positive MBE.

In non-precipitation conditions, the model showed minimal error, with RMSE values less than 1 dBZ, reinforcing its ca-
345   pability to detect the absence of precipitation accurately. The F1 Scores of 0.889, 0.898, and 0.904 for Exp_Baseline_14,
Exp_FullChannel_26, and Exp_PolarDiffEnhanced_35, respectively, confirm the model's efficacy in distinguishing between
precipitating and non-precipitating conditions.

Evaluating the model during extreme precipitation events, such as Typhoon Khanun and the extreme precipitation in Bei-
jing, further demonstrated its precision and robustness. The model effectively reconstructed the overall structure of precipitation
350   systems, with Exp_PolarDiffEnhanced_35 providing the most accurate detail and closely matching actual observations. This
model demonstrated superior performance in reconstructing horizontal distribution, vertical structure, and intensity of reflec-
tivity for both oceanic and terrestrial precipitation. Future work will focus on improving the model with representative training
dataset, more validation and near real-time (NRT) demonstration of derived 3D radar reflectivity.

However, despite these advancements, our study reveals that the resolution of the reconstructed reflectivity from deep learn-
355   ing models does not entirely match the fidelity observed in direct radar measurements. This discrepancy highlights the inherent
challenges in bridging the gap between passive microwave data and active radar observations, largely due to the fundamental
differences in how these instruments collect data. Radiometers receive passive radiation emitted from the Earth's surface and
atmosphere, providing broad and continuous coverage, but with lower spatial and vertical resolution compared to radar obser-
vations. The resolution limitation in passive sensors stems from their reliance on natural radiation signals, such as scattering and
360   thermal emission from clouds, water vapor, precipitation, and the microwave surface emissivity properties, which inherently
have a certain degree of ambiguity (Turk et al., 2018). In contrast, spaceborne precipitation radar directly interacts with atmo-
spheric particles by actively transmitting microwave signals and receiving the power of the microwave signal backscattered by
raindrops, offering detailed insights into the vertical structure of precipitation (Gao et al., 2017). To overcome these limita-
tions, our future work could explore integrating radiometer data with additional datasets, such as information from the FY-3G's
365   onboard sensors like the Medium Resolution Spectral Imager-Rainfall Measurement (MERSI-RM), which is equipped with
eight spectral channels ranging from visible to infrared wavelengths (centered from 0.65 to 12 μm) and has a resolution of 500
meters. These independent ancillary data would enhance the spatial and physical detail available for model training, potentially
improving the accuracy and detail of reconstructed precipitation structures. Furthermore, employing advanced generative mod-

els such as Generative Adversarial Networks (GANs) or diffusion models could provide innovative ways to refine the precision
370   of precipitation reconstructions, leveraging their capacity to generate high-fidelity outputs from relatively coarse inputs (Zhang
et al., 2023b). Thus, while deep learning models offer a robust framework for linking passive and active observational datasets,
the quest to fully replicate the detailed observational capabilities of radar using data from passive sensors continues to pose
significant scientific and technical challenges. Multi-data fusion techniques and advanced modeling approaches may hold the
key to resolving these issues, offering promising avenues for future research in precipitation measurement and modeling.

375   *Code and data availability.*   The code used to train the deep learning models are available at https://doi.org/10.5281/zenodo.13903700. The
training datasets used for this study can be requested from the authors.

Author contributions.   WH, YY conceived the study. YY wrote the first draft. YY and HS contributed to data processing and model training.
JY processed and mapped the ground-based radar data. WH, YY, JL and ZG reviewed and revised the manuscript. WH contributed to
resources. All of the authors read and approved the final manuscript.

380   *Competing interests.*   The contact author has declared that none of the authors has any competing interests.

Acknowledgements.   This study was jointly supported by National Key R&D Program of China(2022YFC3004004) and National Natural
Science Foundation of China (42075155).

References

Bauer, P. and Mugnai, A.: Precipitation profile retrievals using temperature-sounding microwave observations, Journal of Geophysical Research: Atmospheres, 108, https://doi.org/10.1029/2003JD003572, 2003.

Bauer, P., Moreau, E., and Michele, S. D.: Hydrometeor Retrieval Accuracy Using Microwave Window and Sounding Channel Observations, Journal of Applied Meteorology and Climatology, 44, 1016–1032, https://doi.org/10.1175/JAM2257.1, 2005.

Brüning, S., Niebler, S., and Tost, H.: Artificial intelligence (AI)-derived 3D cloud tomography from geostationary 2D satellite data, Atmospheric Measurement Techniques, 17, 961–978, https://doi.org/10.5194/amt-17-961-2024, 2024.

Carminati, F., Atkinson, N., Candy, B., and Lu, Q.: Insights into the Microwave Instruments Onboard the Fengyun 3D Satellite: Data Quality and Assimilation in the Met Office NWP System, Adv. Atmos. Sci., 38, 1379–1396, https://doi.org/10.1007/s00376-020-0010-1, 2021.

Das, S., Wang, Y., Gong, J., Ding, L., Munchak, S. J., Wang, C., Wu, D. L., Liao, L., Olson, W. S., and Barahona, D. O.: A Comprehensive Machine Learning Study to Classify Precipitation Type over Land from Global Precipitation Measurement Microwave Imager (GPM-GMI) Measurements, Remote Sensing, 14, 3631, https://doi.org/10.3390/rs14153631, 2022.

Draper, D. and Newell, D.: Global Precipitation Measurement (GPM) Microwave Imager (GMI) After Four Years On-Orbit, in: 2018 IEEE 15th Specialist Meeting on Microwave Radiometry and Remote Sensing of the Environment (MicroRad), pp. 1–4, https://doi.org/10.1109/MICRORAD.2018.8430702, 2018.

Draper, D. W., Newell, D. A., Wentz, F. J., Krimchansky, S., and Skofronick-Jackson, G. M.: The Global Precipitation Measurement (GPM) Microwave Imager (GMI): Instrument Overview and Early On-Orbit Performance, IEEE Journal of Selected Topics in Applied Earth Observations and Remote Sensing, 8, 3452–3462, https://doi.org/10.1109/JSTARS.2015.2403303, 2015.

Dubovik, O., Schuster, G. L., Xu, F., Hu, Y., Bösch, H., Landgraf, J., and Li, Z.: Grand Challenges in Satellite Remote Sensing, Front. Remote Sens., 2, https://doi.org/10.3389/frsen.2021.619818, 2021.

Fowler, H. J., Blenkinsop, S., Green, A., and Davies, P. A.: Precipitation extremes in 2023, Nat Rev Earth Environ, 5, 250–252, https://doi.org/10.1038/s43017-024-00547-9, 2024.

Gao, J., Tang, G., and Hong, Y.: Similarities and Improvements of GPM Dual-Frequency Precipitation Radar (DPR) upon TRMM Precipitation Radar (PR) in Global Precipitation Rate Estimation, Type Classification and Vertical Profiling, Remote Sensing, 9, 1142, https://doi.org/10.3390/rs9111142, 2017.

Geer, A. J., Bauer, P., Lonitz, K., Barlakas, V., Eriksson, P., Mendrok, J., Doherty, A., Hocking, J., and Chambon, P.: Bulk hydrometeor optical properties for microwave and sub-millimetre radiative transfer in RTTOV-SCATT v13.0, Geoscientific Model Development, 14, 7497–7526, https://doi.org/10.5194/gmd-14-7497-2021, 2021.

Grecu, M., Olson, W. S., and Anagnostou, E. N.: Retrieval of Precipitation Profiles from Multiresolution, Multifrequency Active and Passive Microwave Observations, Journal of Applied Meteorology and Climatology, 43, 562–575, https://doi.org/10.1175/1520-0450(2004)043<0562:ROPPFM>2.0.CO;2, 2004.

Grecu, M., Olson, W. S., Munchak, S. J., Ringerud, S., Liao, L., Haddad, Z., Kelley, B. L., and McLaughlin, S. F.: The GPM Combined Algorithm, Journal of Atmospheric and Oceanic Technology, 33, 2225–2245, https://doi.org/10.1175/JTECH-D-16-0019.1, 2016.

Gu, S., Lu, N., Wu, Q., Yin, H., Sun, F., Chen, L., and Zhang, P.: Analysis and prospect of precipitation detection capability of FY-3 meteorological satellites, Journal of Marine Meteorology, 42, 1–10, 2022.

Guilloteau, C. and Foufoula-Georgiou, E.: Beyond the Pixel: Using Patterns and Multiscale Spatial Information to Improve the Retrieval of Precipitation from Spaceborne Passive Microwave Imagers, Journal of Atmospheric and Oceanic Technology, 37, 1571–1591, https://doi.org/10.1175/JTECH-D-19-0067.1, 2020.

Guilloteau, C., Foufoula-Georgiou, E., Kummerow, C. D., and Petković, V.: Resolving Surface Rain from GMI High-Frequency Channels: Limits Imposed by the Three-Dimensional Structure of Precipitation, Journal of Atmospheric and Oceanic Technology, 35, 1835–1847, https://doi.org/10.1175/JTECH-D-18-0011.1, 2018.

Han, Y., Zou, X., and Weng, F.: Cloud and precipitation features of Super Typhoon Neoguri revealed from dual oxygen absorption band sounding instruments on board FengYun-3C satellite, Geophysical Research Letters, 42, 916–924, https://doi.org/10.1002/2014GL062753, 2015.

Haynes, J. M., Noh, Y.-J., Miller, S. D., Haynes, K. D., Ebert-Uphoff, I., and Heidinger, A.: Low Cloud Detection in Multilayer Scenes Using Satellite Imagery with Machine Learning Methods, Journal of Atmospheric and Oceanic Technology, 39, 319–334, https://doi.org/10.1175/JTECH-D-21-0084.1, 2022.

He, W., Xia, X., Wu, S., Zhang, P., Chen, H., Xia, X., Zhou, Y., and Cai, M.: A rapid assessment of MWRI-RM/FY3G brightness temperature, Atmospheric and Oceanic Science Letters, p. 100466, https://doi.org/10.1016/j.aosl.2024.100466, 2024.

Hou, A. Y., Kakar, R. K., Neeck, S., Azarbarzin, A. A., Kummerow, C. D., Kojima, M., Oki, R., Nakamura, K., and Iguchi, T.: The Global Precipitation Measurement Mission, Bulletin of the American Meteorological Society, 95, 701–722, https://doi.org/10.1175/BAMS-D-13-00164.1, 2014.

Hu, H. and Weng, F.: Influences of 1DVAR Background Covariances and Observation Operators on Retrieving Tropical Cyclone Thermal Structures, Remote Sensing, 14, 1078, https://doi.org/10.3390/rs14051078, 2022.

Huang, Z., Tan, X., Gan, T. Y., Liu, B., and Chen, X.: Thermodynamically enhanced precipitation extremes due to counterbalancing influences of anthropogenic greenhouse gases and aerosols, Nat Water, 1, 614–625, https://doi.org/10.1038/s44221-023-00107-3, 2023.

Kingma, D. P. and Ba, J.: Adam: A Method for Stochastic Optimization, https://doi.org/10.48550/arXiv.1412.6980, 2017.

Kubota, T., Iguchi, T., Kojima, M., Liao, L., Masaki, T., Hanado, H., Meneghini, R., and Oki, R.: A Statistical Method for Reducing Sidelobe Clutter for the Ku-Band Precipitation Radar on board the GPM Core Observatory, Journal of Atmospheric and Oceanic Technology, 33, 1413–1428, https://doi.org/10.1175/JTECH-D-15-0202.1, 2016.

Kummerow, C., Hakkarinen, I. M., Pierce, H. F., and Weinman, J. A.: Determination of Precipitation Profiles from Airborne Passive Microwave Radiometric Measurements, Journal of Atmospheric and Oceanic Technology, 8, 148–158, https://doi.org/10.1175/1520-0426(1991)008<0148:DOPPFA>2.0.CO;2.

Kummerow, C., Barnes, W., Kozu, T., Shiue, J., and Simpson, J.: The Tropical Rainfall Measuring Mission (TRMM) Sensor Package, Journal of Atmospheric and Oceanic Technology, 15, 809–817, https://doi.org/10.1175/1520-0426(1998)015<0809:TTRMMT>2.0.CO;2, 1998.

Laviola, S. and Levizzani, V.: The 183-WSL fast rain rate retrieval algorithm: Part I: Retrieval design, Atmospheric Research, 99, 443–461, https://doi.org/10.1016/j.atmosres.2010.11.013, 2011.

Laviola, S., Levizzani, V., Cattani, E., and Kidd, C.: The 183-WSL fast rain rate retrieval algorithm. Part II: Validation using ground radar measurements, Atmospheric Research, 134, 77–86, https://doi.org/10.1016/j.atmosres.2013.07.013, 2013.

Munchak, S. J. and Skofronick-Jackson, G.: Evaluation of precipitation detection over various surfaces from passive microwave imagers and sounders, Atmospheric Research, 131, 81–94, https://doi.org/10.1016/j.atmosres.2012.10.011, 2013.

Prigent, C., Chevallier, F., Karbou, F., Bauer, P., and Kelly, G.: AMSU-A Land Surface Emissivity Estimation for Numerical Weather
455   Prediction Assimilation Schemes, Journal of Applied Meteorology and Climatology, 44, 416–426, https://doi.org/10.1175/JAM2218.1,
2005.

Qin, L., Chen, Y., Yu, T., Ma, G., Guo, Y., and Zhang, P.: Dynamic Channel Selection of Microwave Temperature Sounding Channels under
Cloudy Conditions, Remote Sensing, 12, 403, https://doi.org/10.3390/rs12030403, 2020.

Shimizu, R., Shige, S., Iguchi, T., Yu, C.-K., and Cheng, L.-W.: Narrowing the Blind Zone of the GPM Dual-Frequency Precipitation Radar
460   to Improve Shallow Precipitation Detection in Mountainous Areas, Journal of Applied Meteorology and Climatology, 62, 1437–1450,
https://doi.org/10.1175/JAMC-D-22-0162.1, 2023.

Simpson, J., Kummerow, C., Tao, W. K., and Adler, R. F.: On the Tropical Rainfall Measuring Mission (TRMM), Meteorl. Atmos. Phys., 60,
19–36, https://doi.org/10.1007/BF01029783, 1996.

Turk, F. J., Haddad, Z. S., Kirstetter, P.-E., You, Y., and Ringerud, S.: An observationally based method for stratifying a priori passive
465   microwave observations in a Bayesian-based precipitation retrieval framework, Quarterly Journal of the Royal Meteorological Society,
144, 145–164, https://doi.org/10.1002/qj.3203, 2018.

Turk, F. J., Ringerud, S. E., Camplani, A., Casella, D., Chase, R. J., Ebtehaj, A., Gong, J., Kulie, M., Liu, G., Milani, L., Panegrossi, G.,
Padullés, R., Rysman, J.-F., Sanò, P., Vahedizade, S., and Wood, N. B.: Applications of a CloudSat-TRMM and CloudSat-GPM Satellite
Coincidence Dataset, Remote Sensing, 13, 2264, https://doi.org/10.3390/rs13122264, 2021.

470 Vakili, M., Ghamsari, M., and Rezaei, M.: Performance Analysis and Comparison of Machine and Deep Learning Algorithms for IoT Data
Classification, https://doi.org/10.48550/arXiv.2001.09636, 2020.

Wang, F., Liu, Y., Zhou, Y., Sun, R., Duan, J., Li, Y., Ding, Q., and Wang, H.: Retrieving Vertical Cloud Radar Reflectivity
from MODIS Cloud Products with CGAN: An Evaluation for Different Cloud Types and Latitudes, Remote Sensing, 15, 816,
https://doi.org/10.3390/rs15030816, 2023a.

475 Wang, Y., Gong, J., Wu, D. L., and Ding, L.: Toward Physics-Informed Neural Networks for 3-D Multilayer Cloud Mask Reconstruction,
IEEE Transactions on Geoscience and Remote Sensing, 61, 1–14, https://doi.org/10.1109/TGRS.2023.3329649, 2023b.

Xie, H., Bi, L., and Han, W.: ZJU-AERO V0.5: An Accurate and Efficient Radar Operator Designed for CMA-GFS/MESO with Capability
of Simulating Non-spherical Hydrometeors, Geoscientific Model Development Discussions, pp. 1–42, https://doi.org/10.5194/gmd-2023-
225, 2024.

480 Yang, Y., Han, W., Sun, H., Xie, H., and Gao, Z.: Reconstruction of 3D DPR Observations Using GMI Radiances, Geophysical Research
Letters, 51, e2023GL106 846, https://doi.org/10.1029/2023GL106846, 2024.

Yuan, Q., Shen, H., Li, T., Li, Z., Li, S., Jiang, Y., Xu, H., Tan, W., Yang, Q., Wang, J., Gao, J., and Zhang, L.:
Deep learning in environmental remote sensing: Achievements and challenges, Remote Sensing of Environment, 241, 111 716,
https://doi.org/https://doi.org/10.1016/j.rse.2020.111716, 2020.

485 Zhang, P., Gu, S., Chen, L., Shang, J., Lin, M., Zhu, A., Yin, H., Wu, Q., Shou, Y., Sun, F., Xu, H., Yang, G., Wang, H., Li, L., Zhang, H.,
Chen, S., and Lu, N.: FY-3G Satellite Instruments and Precipitation Products: First Report of China's Fengyun Rainfall Mission In-Orbit,
Journal of Remote Sensing, 3, 0097, https://doi.org/10.34133/remotesensing.0097, 2023a.

Zhang, Y., Long, M., Chen, K., Xing, L., Jin, R., Jordan, M. I., and Wang, J.: Skilful nowcasting of extreme precipitation with NowcastNet,
Nature, 619, 526–532, https://doi.org/10.1038/s41586-023-06184-4, 2023b.

490 Zhou, W., Guan, H., Li, Z., Shao, Z., and Delavar, M. R.: Remote Sensing Image Retrieval in the Past Decade: Achievements, Challenges, and Future Directions, IEEE Journal of Selected Topics in Applied Earth Observations and Remote Sensing, 16, 1447–1473, https://doi.org/10.1109/JSTARS.2023.3236662, 2023.

Zhu, X. X., Tuia, D., Mou, L., Xia, G.-S., Zhang, L., Xu, F., and Fraundorfer, F.: Deep Learning in Remote Sensing: A Comprehensive Review and List of Resources, IEEE Geoscience and Remote Sensing Magazine, 5, 8–36, https://doi.org/10.1109/MGRS.2017.2762307,
495   2017.